

This work was written as part of one of the author's official duties as an Employee of the United States Government and is therefore a work of the United States Government. In accordance with 17 U.S.C. 105, no copyright protection is available for such works under U.S. Law.

Public Domain Mark 1.0

<https://creativecommons.org/publicdomain/mark/1.0/>

Access to this work was provided by the University of Maryland, Baltimore County (UMBC) ScholarWorks@UMBC digital repository on the Maryland Shared Open Access (MD-SOAR) platform.

Please provide feedback

Please support the ScholarWorks@UMBC repository by emailing scholarworks-group@umbc.edu and telling us what having access to this work means to you and why it's important to you. Thank you.



Water-leaving contribution to polarized radiation field over ocean

PENG-WANG ZHAI,^{1,*} KIRK KNOBELSPIESSE,² AMIR IBRAHIM,^{2,4}
BRYAN A. FRANZ,² YONGXIANG HU,³ MENG GAO,¹ AND ROBERT
FROUIN⁵

¹Department of Physics, University of Maryland Baltimore County, Baltimore, MD 21250, USA

²NASA Goddard Space Flight Center, Code 616, Greenbelt, MD 20771, USA

³MS 475 NASA Langley Research Center, Hampton, VA 23681-2199, USA

⁴Universities Space Research Association, Columbia, MD 21044, USA

⁵Scripps Institution of Oceanography, University of California, San Diego, CA 92093-0224, USA

*pwzhai@umbc.edu

Abstract: The top-of-atmosphere (TOA) radiation field from a coupled atmosphere-ocean system (CAOS) includes contributions from the atmosphere, surface, and water body. Atmospheric correction of ocean color imagery is to retrieve water-leaving radiance from the TOA measurement, from which ocean bio-optical properties can be obtained. Knowledge of the absolute and relative magnitudes of water-leaving signal in the TOA radiation field is important for designing new atmospheric correction algorithms and developing retrieval algorithms for new ocean biogeochemical parameters. In this paper we present a systematic sensitivity study of water-leaving contribution to the TOA radiation field, from 340 nm to 865 nm, with polarization included. Ocean water inherent optical properties are derived from bio-optical models for two kinds of waters, one dominated by phytoplankton (PDW) and the other by non-algae particles (NDW). In addition to elastic scattering, Raman scattering and fluorescence from dissolved organic matter in ocean waters are included. Our sensitivity study shows that the polarized reflectance is minimized for both CAOS and ocean signals in the backscattering half plane, which leads to numerical instability when calculating water leaving relative contribution, the ratio between polarized water leaving and CAOS signals. If the backscattering plane is excluded, the water-leaving polarized signal contributes less than 9% to the TOA polarized reflectance for PDW in the whole spectra. For NDW, the polarized water leaving contribution can be as much as 20% in the wavelength range from 470 to 670 nm. For wavelengths shorter than 452 nm or longer than 865 nm, the water leaving contribution to the TOA polarized reflectance is in general smaller than 5% for NDW. For the TOA total reflectance, the water-leaving contribution has maximum values ranging from 7% to 16% at variable wavelengths from 400 nm to 550 nm from PDW. The water leaving contribution to the TOA total reflectance can be as large as 35% for NDW, which is in general peaked at 550 nm. Both the total and polarized reflectances from water-leaving contributions approach zero in the ultraviolet and near infrared bands. These facts can be used as constraints or guidelines when estimating the water leaving contribution to the TOA reflectance for new atmospheric correction algorithms for ocean color imagery.

© 2017 Optical Society of America

OCIS codes: (010.4450) Oceanic optics; (010.4458) Oceanic scattering; (010.5620) Radiative transfer.

References and links

1. C. R. McClain, "A decade of satellite ocean color observations," *Annual Review of Marine Science* **1**, 19–42 (2009).
2. C. D. Mobley, *Light and Water: Radiative Transfer in Natural Waters* (Academic, 1994).
3. H. R. Gordon and M. Wang, "Retrieval of water-leaving radiance and aerosol optical thickness over the oceans with SeaWiFS: a preliminary algorithm," *Appl. Opt.* **33**, 443–452 (1994).
4. D. Antoine and A. Morel, "A multiple scattering algorithm for atmospheric correction of remotely-sensed ocean colour (MERIS instrument): principle and implementation for atmospheres carrying various aerosols including absorbing ones," *Int. J. Remote Sens.* **20**, 1875–1916 (1999).
5. C. Hu, K. L. Carder, and F. E. Muller-Karger, "Atmospheric correction of SeaWiFS imagery over turbid coastal waters: a practical method," *Remote Sens. Environ.* **74**, 195–206 (2000).

6. D. A. Siegel, M. H. Wang, S. Maritorena, and W. Robinson, "Atmospheric correction of satellite ocean color imagery: the black pixel assumption," *Appl. Opt.* **39**, 3582–3591 (2000).
7. B. Yan, K. Stamnes, W. Li, B. Chen, J. J. Stamnes, and S. C. Tsay, "Pitfalls in atmospheric correction of ocean color imagery: How should aerosol optical properties be computed?," *Appl. Opt.* **41**, 412–423 (2002).
8. H. R. Gordon and K. J. Voss, "MODIS normalized water-leaving radiance algorithm theoretical basis document (MOD 18)," Version 5, May 2004.
http://modis.gsfc.nasa.gov/data/atbd/atbd_mod18.pdf
9. M. H. Wang, and W. Shi, "The NIR-SWIR combined atmospheric correction approach for MODIS ocean color data processing," *Opt. Express* **15**, 15722–15733 (2007).
10. P. J. Werdell, B. A. Franz, and S. W. Bailey, "Evaluation of shortwave infrared atmospheric correction for ocean color remote sensing of Chesapeake Bay," *Rem. Sens. Environ.* **114**, 2238–2247 (2010).
11. S. W. Bailey, B. A. Franz, and P. J. Werdell, "Estimation of near-infrared water-leaving reflectance for satellite ocean color data processing," *Opt. Express* **18**, 7521–7527, (2010).
12. X. He, Y. Bai, D. Pan, J. Tang, and D. Wang, "Atmospheric correction of satellite ocean color imagery using the ultraviolet wavelength for highly turbid waters," *Opt. Express* **20**, 20754–20770, (2012).
13. R. M. Chomko and H. R. Gordon, "Atmospheric correction of ocean color imagery: test of the spectral optimization algorithm with the Sea-viewing Wide Field-of-View Sensor," *Appl. Opt.* **40**, 2973–2984 (2001).
14. C. Shi, T. Nakajima, and M. Hashimoto, "Simultaneous retrieval of aerosol optical thickness and chlorophyll concentration from multiwavelength measurement over East China Sea," *J. Geophys. Res. Atmos.*, **121**, 14084–14101 (2016).
15. J. Chowdhary, B. Cairns, and L. D. Travis, "Contribution of water-leaving radiances to multiangle, multispectral polarimetric observations over the open ocean: bio-optical model results for case 1 waters," *Appl. Opt.* **45** 5542–5567 (2006).
16. O. P. Hasekamp, P. Litvinov, and A. Butz, "Aerosol properties over the ocean from PARASOL multiangle photopolarimetric measurements," *J. Geophys. Res. Atmos.* **116**, D14204 (2011).
17. J. Chowdhary, B. Cairns, F. Waquet, K. Knobelspiesse, M. Ottaviani, J. Redemann, L. Travis, and M. Mishchenko, "Sensitivity of multiangle, multispectral polarimetric remote sensing over open oceans to water-leaving radiance: Analyses of RSP data acquired during the MILAGRO campaign," *Remote Sens. Environ.* **118**, 284–308 (2012).
18. F. Xu, O. Dubovik, P. Zhai, D. J. Diner, O. V. Kalashnikova, F. C. Seidel, P. Litvinov, A. Bovchaliuk, M. J. Garay, G. van Harten, and A. B. Davis, "Joint retrieval of aerosol and water-leaving radiance from multispectral, multiangular and polarimetric measurements over ocean," *Atmos. Meas. Tech.* **9**, 2877–2907 (2016).
19. C. D. Mobley, D. Stramski, W. P. Bissett, and E. Boss, "Optical modeling of ocean waters: Is the case 1 - case 2 classification still useful?" *Oceanography*. **17** 60–67 (2004).
20. M. Chami, Importance of the polarization in the retrieval of oceanic constituents from the remote sensing reflectance, *J. Geophys. Res.* **112**, C05026, (2007).
21. T. Harmel and M. Chami, "Invariance of polarized reflectance measured at the top of atmosphere by PARASOL satellite instrument in the visible range with marine constituents in open ocean waters," *Opt. Express* **16**, 6064–6080 (2008).
22. H. Loisel, L. Duforet, D. Dessailly, M. Chami, and P. Dubuisson, "Investigation of the variations in the water leaving polarized reflectance from the POLDER satellite data over two biogeochemical contrasted oceanic areas," *Opt. Express* **16**, 12905–12918 (2008).
23. X. Q. He, D. L. Pan, Y. Bai, D. F. Wang, and Z. Z. Hao, "A new simple concept for ocean colour remote sensing using parallel polarisation radiance," *Sci. Rep.* **4**, 1–10 (2014).
24. C. Shi, P. C. Wang, T. Nakajima, Y. Ota, S.-C. Tan, and G.-Y. Shi, "Effects of ocean particles on the upwelling radiance and polarized radiance in the atmosphere-ocean system," *Adv. Atmos. Sci.* **32**, 1186–1196 (2015).
25. A. Ibrahim, A. Gilerson, J. Chowdhary, and S. Ahmed, "Retrieval of macro- and micro-physical properties of oceanic hydrosols from polarimetric observations," *Rem. Sens. Environ.* **186**, 548–566 (2016).
26. G. E. Thomas and K. Stamnes, *Radiative Transfer in the Atmosphere and Ocean* (Cambridge University, 1999).
27. Z. Ahmad, and R. S. Fraser, "An iterative radiative transfer code for ocean-atmosphere systems," *J. Atmos. Sci.* **39**, 656–665 (1982).
28. T. Nakajima and M. Tanaka, "Effect of wind-generated waves on the transfer of solar radiation in the atmosphere-ocean system," *J. Quant. Spectrosc. Radiat. Transfer* **29**, 521–537 (1983).
29. J. Fischer and H. Grassl, "Radiative transfer in an atmosphere-ocean system: an azimuthally dependent matrix operator approach," *Appl. Opt.* **23**, 1032–1039 (1984).
30. K. Masuda and T. Takashima, "Computational accuracy of radiation emerging from the ocean surface in the model atmosphere - ocean system," *Pap. Met. Geophys.* **37**, 1–13 (1986).
31. G. W. Kattawar and C. N. Adams, "Stokes vector calculations of the submarine light field in an atmosphere-ocean with scattering according to a Rayleigh phase matrix: effect of interface refractive index on radiance and polarization," *Limnol. Oceanogr.* **34**, 1453–1472 (1989).
32. C. D. Mobley, B. Gentili, H. R. Gordon, Z. Jin, G. W. Kattawar, A. Morel, P. Reinersman, K. Stamnes, and R. H. Stavn, "Comparison of numerical models for computing underwater light fields," *Appl. Opt.* **32**, 7484–7504 (1993).
33. G. W. Kattawar and X. Xu, "Detecting Raman scattering in the ocean by use of polarimetry," *Proc. SPIE* **2258**, 222–233 (1994).

34. H. H. Tynes, G. W. Kattawar, E. P. Zege, I. L. Katsev, A. S. Prikhach, and L. I. Chaikovskaya, "Monte Carlo and multicomponent approximation methods for vector radiative transfer by use of effective Mueller matrix calculations," *Appl. Opt.* **40**, 400–412 (2001).
35. M. Chami, R. Santer, and E. Dilligeard, "Radiative transfer model for the computation of radiance and polarization in an ocean-atmosphere system: polarization properties of suspended matter for remote sensing," *Appl. Opt.* **40**, 2398–2416 (2001).
36. Z. Jin, T. P. Charlock, K. Rutledge, K. Stamnes, and Y. Wang, "Analytical solution of radiative transfer in the coupled atmosphere-ocean system with a rough surface," *Appl. Opt.* **45**, 7443–7455 (2006).
37. R. J. D. Spurr, "LIDORT and VLIDORT. Linearized pseudo-spherical scalar and vector discrete ordinate radiative transfer models for use in remote sensing retrieval problems," in *Light Scattering Reviews*, A. A. Kokhanovsky, ed. (Berlin, 2008), pp. 229–271.
38. P. Zhai, G. W. Kattawar, and P. Yang, "Impulse response solution to the three-dimensional vector radiative transfer equation in atmosphere-ocean systems. I. Monte Carlo method," *Appl. Opt.* **47**, 1037–1047 (2008).
39. P. Zhai, Y. Hu, C. R. Trepte, and P. L. Luckner, "A vector radiative transfer model for coupled atmosphere and ocean systems based on successive order of scattering method," *Opt. Express* **17**, 2057–2079 (2009).
40. P. Zhai, Y. Hu, J. Chowdhary, C. R. Trepte, P. L. Luckner, and D. B. Josset, "A vector radiative transfer model for coupled atmosphere and ocean systems with a rough interface," *J. Quant. Spectrosc. Radiat. Transfer* **111**, 1025–1040 (2010).
41. Ota, Y., A. Higurashi, T. Nakajima, and T. Yokota, "Matrix formulations of radiative transfer including the polarization effect in a coupled atmosphere-ocean system," *J. Quant. Spectrosc. Radiat. Transfer* **111**, 878–894 (2010).
42. A. Hollstein and J. Fischer, "Radiative transfer solutions for coupled atmosphere ocean systems using the matrix operator technique," *J. Quant. Spectrosc. Radiat. Transfer* **113** 536–548 (2012).
43. M. Blum, V.V. Rozanov, J.P. Burrows, and A. Bracher, "Coupled ocean-atmosphere radiative transfer model in the framework of software package SCIATRAN: Selected comparisons to model and satellite data," *Adv. Space Res.* **49**, 1728–1742 (2012).
44. W. Sun and C. Lukashin, "Modeling polarized solar radiation from ocean-atmosphere system for CLARREO inter-calibration applications," *Atmos. Chem. Phys.* **13** 10303–10324 (2013).
45. M. Chami, B. Lafrance, B. Fougne, J. Chowdhary, T. Harmel, and F. Waquet, "OSOAA: a vector radiative transfer model of coupled atmosphere-ocean system for a rough sea surface application to the estimates of the directional variations of the water leaving reflectance to better process multi-angular satellite sensors data over the ocean," *Opt. Express* **23**, 27829–27852 (2015).
46. H. Zheng, "A theoretical study of a vector radiative transfer equation for atmosphere and ocean medium," *IEEE Geosci. Remote Sens. Lett.* **13**, 1430–1432 (2016).
47. A. Tonizzo, M. Twardowski, S. McLean, K. Voss, M. Lewis, and C. Trees, "Closure and uncertainty assessment for ocean color reflectance using measured volume scattering functions and reflective tube absorption coefficients with novel correction for scattering," *Appl. Opt.* **56**, 130–146 (2017).
48. P. Zhai, Y. Hu, D. M. Winker, B. A. Franz, and E. Boss, "Contribution of Raman scattering to polarized radiation field in ocean waters," *Opt. Express* **23**, 23582–23596 (2015).
49. P. Zhai, Y. Hu, D. M. Winker, B. A. Franz, P. J. Werdell, and E. Boss, "Inelastic vector radiative transfer solution in ocean waters," *Opt. Express* **25**, A223–A239 (2017).
50. G. Thuillier, M. Herse, S. Labs, T. Foujols, W. Peetermans, D. Gillotay, P.C. Simon, and H. Mandel, "The solar spectral irradiance from 200 to 2400 nm as measured by SOLSPEC Spectrometer from the ATLAS 123 and EURECA missions," *Solar Physics* **214** 1–22 (2003).
51. Z. Ahmad, B. A. Franz, C. R. McClain, E. J. Kwiatkowska, J. Werdell, E. P. Shettle, and B. N. Holben, "New aerosol models for the retrieval of aerosol optical thickness and normalized water-leaving radiances from the SeaWiFS and MODIS sensors over coastal regions and open oceans," *Appl. Opt.* **49**, 5545–5560 (2010).
52. N. Braslau and J. V. Dave, "Effect of aerosols on the transfer of solar energy through realistic model atmospheres. part I: non-absorbing aerosols," *J. Appl. Meteor.* **12**, 601–615 (1973).
53. Committee on Extension to the Standard Atmosphere, *U. S. standard atmosphere*, (U.S. Government Printing Office, Washington D.C. 1976).
54. C. Tomasi, V. Vitale, B. Petkov, A. Lupi, and A. Cacciari, "Improved algorithm for calculations of Rayleigh-scattering optical depth in standard atmospheres," *Appl. Opt.* **44**, 3320–3341 (2005).
55. J. E. Hansen and L. D. Travis, "Light scattering in planetary atmospheres," *Space Sci. Rev.* **16**, 527–610 (1974).
56. S. A. Buehler, P. Eriksson, T. Kuhn, A. von Engeln and C. Verdes "ARTS, the Atmospheric Radiative Transfer Simulator," *J. Quant. Spectrosc. Radiat. Transfer* **91**, 65–93 (2005).
57. P. Eriksson, S. A. Buehler, C. P. Davis, C. Emde, and O. Lemke, "ARTS, the atmospheric radiative transfer simulator, Version 2," *J. Quant. Spectrosc. Radiat. Transfer* **112**, 1551–1558 (2011).
58. L.S. Rothman, I.E. Gordon, Y. Babikov, A. Barbe, D. Chris Benner, P.F. Bernath, M. Birk, L. Bizzocchi, V. Boudon, L.R. Brown, A. Campargue, K. Chance, E.A. Cohen, L.H. Coudert, V.M. Devi, B.J. Drouin, A. Fayt, J.-M. Flaud, R.R. Gamache, J.J. Harrison, J.-M. Hartmann, C. Hill, J.T. Hodges, D. Jacquemart, A. Jolly, J. Lamouroux, R.J. Le Roy, G. Li, D.A. Long, O.M. Lyulin, C.J. Mackie, S.T. Massie, S. Mikhailenko, H.S.P. Müller, O.V. Naumenko, A.V. Nikitin, J. Orphal, V. Perevalov, A. Perrin, E.R. Polovtseva, C. Richard, M.A.H. Smith, E. Starikova, K. Sung, S. Tashkun, J. Tennyson, G.C. Toon, V.I.G. Tyuterev, and G. Wagner, "The HITRAN2012 molecular spectroscopic

- database," J. Quant. Spectrosc. Radiat. Transfer **130**, 4–50 (2013).
59. C. Cox and W. Munk, "Measurement of the roughness of the sea surface from photographs of the suns glitter," J. Opt. Soc. Am. **44**, 838–850 (1954).
 60. L. Kou, D. Labrie, and P. Chylek, "Refractive indices of water and ice in the 0.65–2.5 μ m spectral range," Appl. Opt. **32**, 3531–3540 (1993).
 61. R. M. Pope and E. S. Fry, "Absorption spectrum (380–700 nm) of pure water. II Integrating measurements," Appl. Opt. **36**, 8710–8723 (1997).
 62. X. Zhang and L. Hu, "Scattering by pure seawater at high salinity," Opt. Express **17**, 12685–12691 (2009).
 63. A. Bricaud, A. Morel, M. Babin, K. Allali, and H. Claustre, "Variations of light absorption by suspended particles with chlorophyll a concentration in oceanic (case 1) waters: analysis and implications for bio-optical models," J. Geophys. Res. **103**, 31033–31044 (1998).
 64. Bricaud, A., M. Babin, H. Claustre, J. Ras, and F. Tière, "Light absorption properties and absorption budget of Southeast Pacific waters," J. Geophys. Res. **115**, C08009 (2010).
 65. K. J. Voss, "A spectral model of the beam attenuation coefficient in the ocean and coastal areas," Limnol. Oceanogr. **37**, 501–509, (1992).
 66. IOCCG Ocean Color Algorithm Working Group, "Models, parameters, and approaches that used to generate wide range of absorption and backscattering spectra," (2003).
 67. G. Fourier and J. L. Forand, "Analytic phase function for ocean water," Proc. SPIE **2258**, 194–201 (1994).
 68. G. Fournier and M. Jonasz, "Computer-based underwater imaging analysis," Proc. SPIE **3761**, 62–70 (1999).
 69. C. D. Mobley, L. K. Sundman, E. Boss, "Phase function effects on oceanic light fields," Appl. Opt. **41**, 1035–1050 (2002).
 70. Y. Huot, A. Morel, M. S. Twardowski, D. Stramski, and R. A. Reynolds, "Particle optical backscattering along a chlorophyll gradient in the upper layer of the eastern South Pacific Ocean," Biogeosciences **5**, 495–507 (2008).
 71. A. Morel and B. Gentili, "A simple band ratio technique to quantify the colored dissolved and detrital organic material from ocean color remotely sensed data," Rem. Sens. Environ. **113**, 998–1011 (2009).
 72. K. J. Voss and E. S. Fry, "Measurement of the Mueller matrix for ocean water," Appl. Opt. **23**, 4427–4439 (1984).
 73. A. A. Kokhanovsky, "Parameterization of the Mueller matrix of oceanic waters," J. Geophys. Res. **108**, 3175 (2003).
 74. C. Áurea, L. R. Marlon, and C. J. John, "Assessment of the relationships between dominant cell size in natural phytoplankton communities and the spectral shape of the absorption coefficient, Limnol. Oceanogr., **47**, 404–417 (2002).
 75. M. Jonasz and G. Fournier, *Light Scattering by Particles in Water: Theoretical and Experimental Foundations* (Academic, 2007).
 76. M. Babin, D. Stramski, G. M. Ferrari, H. Claustre, A. Bricaud, G. Obolensky, and N. Hoepffner, "Variations in the light absorption coefficients of phytoplankton, nonalgal particles, and dissolved organic matter in coastal waters around Europe," J. Geophys. Res. **108**, 3211, (2003).
 77. S. B. Wozniak and D. Stramski, "Modeling the optical properties of mineral particles suspended in seawater and their influence on ocean reflectance and chlorophyll estimation from remote sensing algorithms," Appl. Opt. **43**, 3489–3503 (2004).
 78. D. Doxaran, K. Ruddick, D. McKee, B. Gentili, D. Tailliez, M. Chami, and M. Babin, "Spectral variations of light scattering by marine particles in coastal waters, from visible to near infrared," Limnol. Oceanogr. **54**, 1257–1271 (2009).
 79. M. I. Mishchenko, L. D. Travis, and A. A. Lacis, *Scattering, Absorption, and Emission of Light by Small Particles* (Cambridge University, 2002).
 80. G. E. Walrafen, "Raman spectral studies of effects of temperature on water structure," J. Chem. Phys. **47**, 114–126 (1967).
 81. S. Sugihara, M. Kishino, and N. Okami, "Contribution of Raman scattering to upward irradiance in the sea," J. Oceanogr. Soc. Jpn. **40**, 397–404 (1984).
 82. R. H. Stavn and A. D. Weidemann, "Optical modeling of clear ocean light fields: Raman scattering effects," Appl. Opt. **27**, 4002–4011 (1988).
 83. B. R. Marshall and R. C. Smith, "Raman scattering and in-water ocean optical properties," Appl. Opt. **29**, 71–84 (1990).
 84. Y. Ge, K. J. Voss, and H. R. Gordon, "In situ measurements of inelastic scattering in Monterey Bay using solar Fraunhofer lines," J. Geophys. Res. **100**, 13227–13236 (1995).
 85. K. J. Waters, "Effects of Raman scattering on water-leaving radiance," J. Geophys. Res. **100**, 13151–13161 (1995).
 86. C. M. Hu and K. J. Voss, "In situ measurements of Raman scattering in clear ocean water," Appl. Opt. **36**, 6962–6967 (1997).
 87. J. S. Bartlett, K. J. Voss, S. Sathyendranath, and A. Vodacek, "Raman scattering by pure water and seawater," Appl. Opt. **37**, 3324–3332 (1998).
 88. H. R. Gordon, "Contribution of Raman scattering to water-leaving radiance: a reexamination," Appl. Opt. **38**, 3166–3174 (1999).
 89. H. R. Gordon, M. R. Lewis, S. D. McLean, M. S. Twardowski, S. A. Freeman, K. J. Voss, and G. C. Boynton, "Spectra of particulate backscattering in natural waters," Opt. Express **17**, 16192–16208 (2009).
 90. T. K. Westberry, E. Boss, and Z.-P. Lee, "Influence of Raman scattering on ocean color inversion models," Appl. Opt.

- 52, 5552–5561 (2013).
91. S. K. Hawes, C. K. Carder, and G. R. Harvey, “Quantum fluorescence efficiencies of fulvic and humic acids: effects on ocean color and fluorometric detection,” in *Ocean Optics XI*, G. D. Gilbert, ed., Proc. SPIE 1750, 212–223 (1992).
 92. S. A. Green and N. V. Blough, “Optical absorption and fluorescence properties of chromophoric dissolved organic matter in natural waters,” *Limnol. Oceanogr.* **39**, 1903–1916 (1994).
 93. A. Vodacek, N. V. Blough, M. D. DeGrandpre, E. T. Peltzer, and R. K. Nelson, “Seasonal variation of CDOM and DOC in the Middle Atlantic Bight: terrestrial inputs and photooxidation,” *Limnol. Oceanogr.* **42**, 674–686 (1997).
 94. D. Pozdiakov and H. Grassl, *Color of Inland and Coastal Waters: A Methodology for its Interpretation* (Springer-Praxis, 2003).
 95. J. Vigneshwaran, P. Shanmugam and E. A. Gokul, “Simulating the effects of inelastic scattering on upwelling radiance in coastal and inland waters: implications for hyperspectral remote sensing,” *Current Science* **108**, 903–914, (2015).
 96. A. Wolanin, V. Rozanov, T. Dinter, and A. Bracher, “Detecting CDOM fluorescence using high spectrally resolved satellite data: a model study,” in *Towards an Interdisciplinary Approach in Earth System Science*, G. Lohmann, H. Meggers, V. Unnithan, D. Wolf-Gladrow, J. Notholt and A. Bracher, eds. (Springer, 2015), p. 251
 97. H. R. Gordon, “The diffuse reflectance of the ocean: the theory of its augmentation by chlorophyll a fluorescence at 685 nm,” *Appl. Opt.* **18**, 1161–1166 (1979).
 98. R. W. Preisendorfer and C. D. Mobley, “Theory of fluorescent irradiance fields in natural waters,” *J. Geophys. Res.* **93D**, 10831–10855 (1988).
 99. A. M. Kouassi, R. G. Zika, and J. M. C. Plane, “Light-induced alteration of the photophysical properties of dissolved organic matter in sea water,” *Neth. J. Sea Res.* **27**, 33–41 (1990).
 100. Y. T. Ge, H. R. Gordon, and K. J. Voss, “Simulation of inelastic scattering contributions to the irradiance field in the ocean: variation in Fraunhofer line depths,” *Appl. Opt.* **32**, 4028–4036 (1993).
 101. M. Schroeder, H. Barth, and R. Reuter, “Effect of inelastic scattering on underwater daylight in the ocean: model evaluation, validation, and first results,” *Appl. Opt.* **42**, 4244–4260 (2003).
 102. M. J. Behrenfeld, T. K. Westberry, E. S. Boss, R. T. O’Malley, D. A. Siegel, J. D. Wiggert, B. A. Franz, C. R. McClain, G. C. Feldman, S. C. Doney, J. K. Moore, G. Dall’Olmo, A. J. Milligan, I. Lima, and N. Mahowald, “Satellite-detected fluorescence reveals global physiology of ocean phytoplankton,” *Biogeosciences* **6**, 779–794, (2009).
 103. J. R. Morrison, “In situ determination of the quantum yield of phytoplankton chlorophyll a fluorescence: A simple algorithm, observations, and a model,” *Limnol. Oceanogr.* **48**, 618–631 (2003).
 104. J. Uitz, H. Claustre, A. Morel, and S. B. Hooker, “Vertical distribution of phytoplankton communities in open ocean: An assessment based on surface chlorophyll,” *J. Geophys. Res.* **111**, C08005, (2006).
 105. A. Morel and J. F. Berton, “Surface pigments, algal biomass profiles, and potential production of the euphotic layer: Relationships reinvestigated in view of remote-sensing applications,” *Limnol. Oceanogr.* **34**, 1545–1562 (1989).
 106. Y. Kawata, “Circular polarization of sunlight reflected by planetary atmospheres,” *Icarus* **33**, 217–232 (1978).
 107. M. Gao, X. Huang, P. Yang, and G. W. Kattawar, “Angular distribution of diffuse reflectance from incoherent multiple scattering in turbid media,” *Appl. Opt.* **52**, 5869–5879 (2013).

1. Introduction

Ocean color remote sensing is an important tool for monitoring global ocean productivity and environmental health [1]. An ocean color satellite-borne sensor measures the total radiance at the top of the atmosphere (TOA) from the coupled atmosphere and ocean system (CAOS), which includes contributions from the atmosphere, ocean surface, and ocean water body [2]. Atmospheric correction algorithms have been developed to remove the atmosphere and surface contributions to obtain the water-leaving radiance [3–10]. Traditionally, atmospheric correction algorithms assume negligible water-leaving radiance in the near infrared (NIR), which allows the aerosol type and loading to be determined in NIR and extrapolated into visible [3]. This strategy is highly successful in open ocean, however, its application is limited for scenes involving either turbid ocean waters in which the NIR water-leaving radiance is not zero, or absorbing aerosols in which extrapolation from NIR to visible is questionable [6, 8].

Several algorithms have been proposed to improve atmospheric corrections for these scenes. One scheme assumes negligible water-leaving radiance in the shortwave infrared (SWIR) bands [9]. Werdell et al. have shown that the SWIR scheme leads to significant errors for shorter wavelengths at 555 nm or 443 nm due to the large spectral range of data extrapolation and insufficient signal to noise ratios (SNR) in the SWIR [10]. Another method is to estimate water-leaving radiance in NIR iteratively for turbid waters (see [11], and references within). In the

above NIR or SWIR methods extrapolation has to been done to derive aerosol properties in the visible from longer wavelengths. He et al. have proposed an atmospheric correction scheme that assumes water-leaving radiance in ultraviolet (UV) is negligible due to the high concentration and large absorption coefficient of colored dissolved organic matter (CDOM) [12]. In this scheme the aerosol properties can be interpolated between UV and NIR. However, atmospheric correction using the UV bands is difficult because molecular scattering is large, coupling between particle absorption and scattering is significant, and aerosol height distribution has large influences to the measurement. In order to develop efficient atmospheric correction schemes, the water leaving contribution to the TOA total measurement should be examined and well understood. However, the magnitude of the water-leaving radiance in UV for a variety of waters has not been demonstrated yet.

Other methods have been proposed to retrieve water-leaving radiance and aerosol properties jointly using the least squares fitting of the TOA radiance in combination with ocean bio-optical models [13, 14]. In recent years, the aerosol and ocean color joint retrieval has been advanced using multi-angle polarized measurements at multiple wavelengths [15–18]. Overall the joint retrieval methods can be called 1-step approaches, while the traditional methods assuming negligible water-leaving radiance in NIR or SWIR can be regarded as 2-step approaches. The 1-step approaches have the advantage of addressing absorbing aerosols if the inherent optical properties (IOPs) of ocean waters can be adequately represented by bio-optical models. On the other hand, the 2-step approaches are numerically efficient and physically sound with a limited number of assumptions about ocean water reflectance. Consequently, the 2-step approaches are the robust and reliable source of global data on ocean biology and biogeochemistry research today.

To further advance the research of atmospheric correction for ocean color imagery, it is important to understand the water leaving contribution to the TOA radiance. Chowdhary et al. have studied the magnitude and angular variation of the total and polarized water-leaving reflectances based on bio-optical models of case 1 waters, in which IOPs are parameterized solely in terms of chlorophyll concentration [15]. The wavelength range was from 400 nm to 600 nm and for chlorophyll a concentration from 0.03 to 3.0 mg/m³. The case 1 and case 2 classification of ocean waters has been under debate in the ocean optics community [19]. In this paper, we use the term of case 1 and case 2 classification in the same sense of what was used in the cited references. Chami has studied the importance of the TOA polarized reflectance to both open ocean and coastal waters [20]. The wavelength range was from 443 to 870 nm. Chami suggested that polarized signals can be used for atmospheric correction because the TOA polarized signals are insensitive to open ocean water properties. This has been verified by the PARASOL (Polarization and Anisotropy of Reflectance for Atmospheric Sciences coupled with Observations from a Lidar) measurement [21]. This is however not true for bright waters dominated by algal blooms or sediments [20, 22]. He et al. have studied the water-leaving contribution to the TOA polarized reflectance at 443 nm and 670 nm for the purpose of using parallel polarization for ocean color retrieval [23]. Shi et al. have shown the impacts of ocean particle properties on the radiation field at three levels: just below the water surface, just above the water surface, and TOA [24]. Ibrahim et al. have also shown the responses of TOA degree of linear polarization to both case 1 and case 2 waters at 440, 550, and 665 nm [25].

To date the water-leaving contribution to the TOA radiation field has not been explored in UV, which is critical to develop advanced atmospheric correction algorithms using the UV wavelengths. The sensitivity study of water-leaving contribution to the TOA radiation field relies on the theoretical radiative transfer models for CAOS [26–47]. The TOA water-leaving contribution studies [15, 20, 24] outlined above did not include the inelastic scattering in the VRT models. In this paper we systematically studied the water leaving contribution to the TOA radiation field, for both the total and polarized reflectance, in the spectral range from

UV to NIR, with a focus on understanding the magnitude and angular variation of the water-leaving contribution in the UV and blue wavelengths for two types of waters, one dominated by phytoplankton and the other by non-algae (i.e., mineral sediment) particles (NAP). The water leaving radiances in shortwave infrared bands are not included in this study because they are essentially zero due to large water absorption. Both elastic and inelastic scattering are included in the vector radiative transfer simulation [48,49]. This work will pave the path for new atmospheric correction algorithms using the UV channels.

This paper is organized as follows: Sec. 2 describes the radiative transfer model and the single scattering properties of atmosphere and ocean systems for two types of waters, one is dominated by phytoplankton and the other by NAP; Sec. 3 shows the simulation result and discussion; Sec. 4 summarizes the conclusions based on the simulation.

2. Radiative transfer model and bio-optical models

The radiative transfer model used in this study is the vector radiative transfer model for CAOS based on the successive order or scattering (SOS) method [39,40,48,49]. The SOS code assumes plane-parallel geometry and accounts for polarization, atmosphere and ocean coupling, elastic and inelastic scattering. The major inelastic scattering mechanisms include ocean water Raman scattering, fluorescence of dissolved organic matter (FDOM), and chlorophyll fluorescence [48,49]. The SOS code has been validated against other radiative transfer models, including the matrix operator method [15] and the Monte Carlo method [38]. To simulate inelastic scattering, we need the solar spectral irradiance and single scattering optical properties for both aerosols and hydrosols for the whole spectrum from UV to NIR. In this work, the solar spectral irradiance is from [50]. The atmosphere is assumed to be a mixture of aerosols and molecules. The aerosol model used is taken from Ahmad et al. [51] with a fine-mode volume fraction of 20% and relative humidity of 80%. This aerosol model is weakly absorbing with the single scattering albedo around 0.98 from 340 nm to 865 nm. The aerosol vertical distribution is from [52]. An aerosol optical depth of 0.15 at 550nm is used and a larger optical depth will reduce the TOA water leaving signal. The molecules vertical profile is the 1976 US standard atmosphere [53] with optical depth determined by [54]. The molecular scattering is described by the Rayleigh scattering matrix with a depolarization of 0.0284 [55].

Water vapor absorption has been considered in order to properly calculate the inelastic source function for Raman scattering and FDOM. The water vapor volume mixing ratio is around 2.5% at the surface, decreasing to 1% at 2.5 km and almost zero at 10 km. The atmospheric radiative transfer simulator (ARTS) is used to calculate the water vapor absorption coefficient [56,57] with the water vapor line parameters based on the high-resolution transmission molecular absorption database (HITRAN) [58]. The water vapor absorption coefficient is calculated from 300 nm to 900 nm with spectral resolution of 1 nm, which is then averaged to 5 nm when calculating the inelastic source function in ocean inelastic scattering. Other gas absorption in the atmosphere is ignored due to their generally weak contribution in the wavelengths considered. The absorbing effect of ozone was not considered in our calculations for simplicity. While ozone absorption can lead to as much as a 10% reduction in visible radiance scattered into the satellite sensor field of view, this absorption occurs high in the atmosphere where coupling between scattering and absorption is minimal. As such, ozone absorption impacts the ocean and atmosphere signal equally, and thus it will not significantly impact the fractional contribution of water leaving radiance to top of atmosphere radiance. The ocean surface roughness is specified by the Cox-Munk model [59], with the wind speed of 5m/s. The dependence of ocean roughness on wind direction is neglected.

The ocean water IOPs are derived from bio-optical models for two kinds of waters, one dominated by phytoplankton and the other by NAP. For waters dominated by phytoplankton particles, ocean water is consisted of three components: pure sea water, chlorophyll a covariant

phytoplankton particles, and colored dissolved organic matter (CDOM). The absorption coefficient a_w of pure sea water is from measurements in [60,61]. The scattering coefficient b_w of pure sea water is based on [2,62] without considering the dependence on salinity and temperature. The IOPs of phytoplankton particles are parameterized in terms of chlorophyll concentration [Chla]. The absorption coefficients a_p of phytoplankton particles is from [63], which is valid between 400 nm and 700 nm. The a_p value for $\lambda < 400$ nm is from the measurement in the BIOSOPE field campaign [64], which is rescaled to make sure a_p is continuous at 440 nm with [63]. The phytoplankton scattering coefficient $b_p = c_p - a_p$, with c_p takes the same format as in [49], which is based on [65,66]. The phytoplankton phase function is the Fourier-Forand (FF) phase function determined by the backscattering ratio $B_{bp} = b_{bp}/b_p$ [67–69]. The backscattering ratio B_{bp} is spectrally flat and only depends on [Chla] [70]. The FF phase function is then mixed with pure sea water phase function weighted by their scattering coefficients. The scattering coefficient of the CDOM is assumed to be negligible and its absorption coefficient $a_y = a_{y,440} \exp[-S(\lambda - 440)]$, with $S=0.018$ [71] and $a_{y,440}$ covariant with a_p at 440 nm [49,66]. The Mueller matrix of phytoplankton dominated waters is expressed as a product of the FF function and the reduced Mueller matrix from [72,73]. Hereafter we refer this first water type as phytoplankton dominated waters (PDW), whose bio-optical model has been described in greater details in [49].

The second water type is dominated by NAP, which is referred to as NDW hereafter. NDW is consisted of four components: pure sea water, chlorophyll a covariant phytoplankton particles, CDOM and NAP. The IOPs of pure sea water and CDOM are the same as PDW, while the phytoplankton particles are however modeled differently. The absorption coefficient of phytoplankton particles in NDW is modeled as a linear combination of micro- and pico- plankton particles weighted by parameter S_f [74]. In this study we adopted $S_f = 0.287$ among other values in [74]. For wavelengths shorter than 400 nm, the BIOSOPE measurement is again used [64], in a way similar to PDW. The scattering coefficient of phytoplankton particle is $b_p = c_p - a_p$, with c_p determined from [65]. The Mueller matrix of the phytoplankton particle is determined by spherical particles with Junge particle size distribution (PSD). The index of refraction of phytoplankton particle is $n_p = 1.06$ relative to water; and the Junge PSD slope is $\xi_p = 4$ [75]. The NAP absorption coefficient is modeled as $a_{NAP} = a_{NAP}(443)\{0.75 \exp[-0.0123(\lambda - 443)]\}$ with $a_{NAP}(443) = 0.041[NAP]$, where [NAP] is the NAP concentration in the unit of g/m^3 [76]. The NAP scattering coefficient b_{NAP} is determined by the spherical particle scattering cross section with Junge particle size distribution (see Eqs. 4 - 6 of [25,77]). The spectral backscattering coefficient calculated from the Mie theory assuming zero imaginary index of refraction can be 5% to 30% higher than the field measurements [78]. We have adopted an empirical correction scheme to correct this artifact (see Eq. (13), [78]). The NAP Mueller matrix is also modeled by the spherical particles with Junge PSD. The NAP index of refraction is $n_{NAP} = 1.2$ relative to water; and the Junge PSD slope is $\xi_{NAP} = 4$ [75]. The Mie code used here is developed by Mishchenko et al. [79]. A more detailed description of the NDW bio-optical model has been provided in [25], in which NDW is referred as case 2 waters.

The SOS code is used to simulate the polarized radiation field at TOA in the following discrete wavelengths: 340 nm, 354 nm, 388 nm, 416 nm, 442 nm, 452 nm, 470 nm, 510 nm, 551 nm, 670 nm, 765 nm, and 865 nm, which covers the spectral range from UV to NIR in which water leaving radiance is significant. All inelastic scattering mechanisms for ocean waters have been accounted for, which include Raman scattering [33,48,80–90], FDOM [91–96], and chlorophyll fluorescence [97–103]. Chlorophyll fluorescence is only significant near the wavelength of 685 nm, which we did not include in this work. For details of the inelastic scattering implementation, readers are referred to [48,49]. The vertical profile of the chlorophyll a concentration [Chla] is a generalized Gaussian superposed to a linear background [104,105], which can be uniquely determined by the [Chla] at the surface [49]. Hereafter we refer [Chla] to the surface chlorophyll a concentration. The non-algae concentration [NAP] is considered uniform within the water

column. The simulation assumes that the total ocean depth is 200 meter without ocean bottom reflection, which is deep enough for water leaving radiance to converge at the TOA.

3. Simulations and discussion

In this section we studied the radiation field at the TOA in response to different [Chla] and [NAP] values. The total reflectance ρ_t is defined as:

$$\rho_t = \frac{\pi L_t(\lambda, \theta_s, \theta_v, \phi_v)}{E_s(\lambda) \cos \theta_s}, \quad (1)$$

where L_t is the TOA radiance; E_s is the extraterrestrial solar irradiance; λ is the wavelength; θ_s and θ_v are the solar and viewing zenith angles, respectively; ϕ_v is the viewing azimuth angle. In this paper $\theta_s = 45^\circ$ is used. The range of the viewing angle covers all upwelling direction at the TOA. The total reflectance ρ_t is a summation of signals from all components of CAOS. The water-leaving signal ρ'_w in the TOA reflectance is:

$$\rho'_w = \frac{\pi L'_w(\lambda, \theta_s, \theta_v, \phi_v)}{E_s(\lambda) \cos \theta_s}, \quad (2)$$

where L'_w is the water-leaving radiance contribution at the TOA. L_w is not used here because it is conventionally used to denote water leaving radiance just above the ocean surface. In this work L'_w is calculated by

$$\mathbf{L}'_w = \mathbf{L}_t - \mathbf{L}_{t, w/o \text{ water}} \quad (3)$$

where \mathbf{L} is the Stokes vector and $\mathbf{L}_{t, w/o \text{ water}}$ denotes the TOA measurement for a system with the same atmosphere and ocean surface but no ocean water is present. Radiance L is the first element of \mathbf{L} , and Q and U used in the following are the second and third elements. Equation (3) accounts for all multiple scattering and polarization effects in the atmosphere and ocean coupled system.

To study the polarized radiation field, the linearly polarized reflectance is introduced, for both the total and water-leaving signals:

$$\begin{aligned} \rho_{t, pol} &= \frac{\pi \sqrt{Q_t^2(\lambda, \theta_s, \theta_v, \phi_v) + U_t^2(\lambda, \theta_s, \theta_v, \phi_v)}}{E_s(\lambda) \cos \theta_s}, \\ \rho'_{w, pol} &= \frac{\pi \sqrt{Q_w'^2(\lambda, \theta_s, \theta_v, \phi_v) + U_w'^2(\lambda, \theta_s, \theta_v, \phi_v)}}{E_s(\lambda) \cos \theta_s}, \end{aligned} \quad (4)$$

where subscripts t and w represent the total and water-leaving signals, respectively. The calculation of Q'_w and U'_w follows Eq. (3). Hereafter the linearly polarized reflectance is called the polarized reflectance for conciseness, as the circular component is generally small in the TOA measurement [106]. In the above reflectance quantities, the spectral variation of the radiation field due to the solar irradiance is largely removed so that they are mainly sensitive to the atmospheric and oceanic IOPs. We have also defined the relative contributions of the total and polarized water leaving signal at the TOA in the following way:

$$\begin{aligned} \eta &= 100 \cdot \rho'_w / \rho_t, \\ \eta_{pol} &= 100 \cdot \rho'_{w, pol} / \rho_{t, pol} \end{aligned} \quad (5)$$

3.1. Total reflectance

Figures 1(a) and 1(b) show the TOA reflectance ρ_t and ρ'_w at the nadir viewing angle for PDW and NDW, respectively. The solar zenith angle is 45° and the aerosol optical depth τ_a at 550

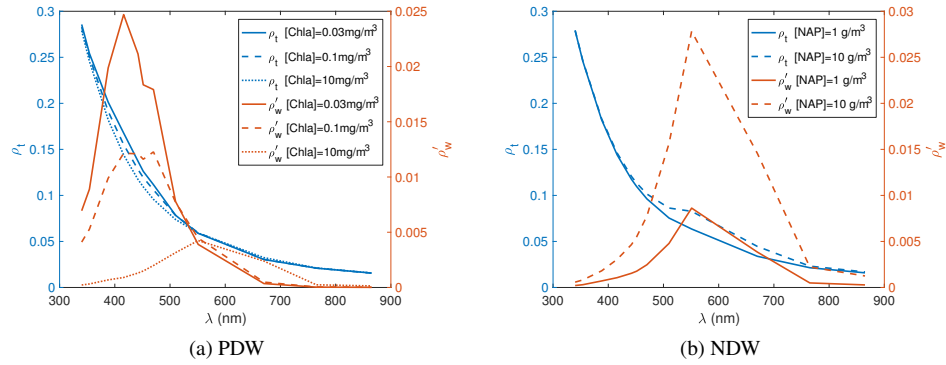


Fig. 1. TOA Reflectance at nadir as a function of wavelength. The total reflectance is shown in blue by the left y axis and the water leaving signal is shown in maroon by the right y axis. This arrangement applies to all other similar plots in this paper. The solar zenith angle is 45° and the aerosol optical depth at 550 nm is 0.15.

nm is 0.15. For PDW, three [Chla] values are used: 0.03, 0.1, and 10 mg/m^3 . For NDW, the chlorophyll a concentration is fixed at $[\text{Chla}] = 10.0 \text{ mg/m}^3$ and two [NAP] values are used: 1 and 10 g/m^3 . In all cases, the total reflectance ρ_t , which includes contributions from both the atmosphere and ocean, increases with decreasing wavelength. This is mainly due to the increase of molecular and aerosol scattering as wavelength decreases. The water-leaving signal in the total reflectance is noticeable from Fig. 1 between 400 nm and 600 nm for both PDW and NDW, the signal from NDW being more prominent.

For PDW, there is an inflection wavelength between 510 nm and 550 nm where the ρ'_w values for different [Chla] values are comparable. When wavelength is shorter than this inflection wavelength, the water-leaving signal ρ'_w is larger for smaller [Chla] values. This trend is reversed if wavelength is longer than the inflection wavelength. This is due to the compound effect of spectral variations of the backscattering and absorption coefficients, which has led to similar spectral behavior of irradiance reflectance in [17]. As [Chla] increases from 0.03 to 10 mg/m^3 for PDW, the wavelength of the ρ'_w maximum shifts from around 412 nm to 550 nm. For $[\text{Chla}] = 0.03$ and 0.1 mg/m^3 , ρ'_w has a local minimum around 442 nm, which is from the compound effect of the total absorption and backscattering coefficient spectra. The water-leaving signal ρ'_w decreases as wavelength approaches both UV and NIR at both sides of the maximum for all chlorophyll a concentrations. The ρ'_w maximum value ranges from 0.025 to 0.005 as [Chla] changes from 0.03 to 10 mg/m^3 .

Different from PDW, the NDW water-leaving signal ρ'_w does not have an inflection wavelength, at which the relative magnitude of ρ'_w changes for different [NAP] values. The NDW water-leaving signal is larger for larger [NAP] across the whole spectrum. The wavelength of the ρ'_w maximum is not sensitive to [NAP]. For both PDW and NDW, the ρ'_w values are smaller in both UV and NIR than in the visible bands, which is the basis of atmospheric correction using the UV and NIR bands. The reflectance ρ'_w at 865 nm for $[\text{NAP}] = 10 \text{ g/m}^3$ is around 0.001, which is small but not negligible in terms of atmospheric correction. At 340 nm, ρ'_w is around the same level as NIR.

Besides the spectral variation, another important property of the radiation field is the angular distribution. Figure 2 displays the fisheye projection of TOA reflectance ρ_t and ρ'_w contour at 354 nm for both PDW and NDW, respectively. In the plot the radial coordinate represents the

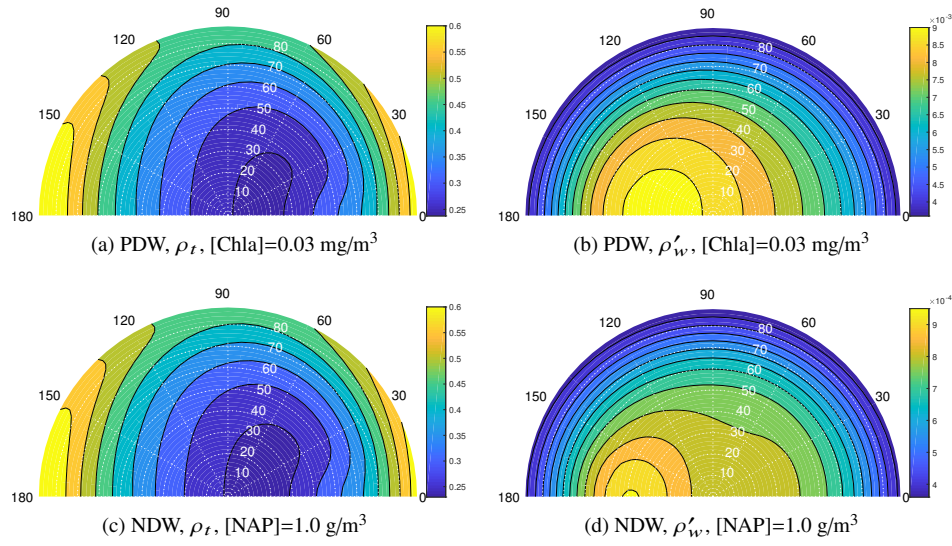


Fig. 2. Fisheye projection of TOA reflectance contour at 354 nm. The solar zenith angle is 45° and the aerosol optical depth at 550 nm is 0.15.

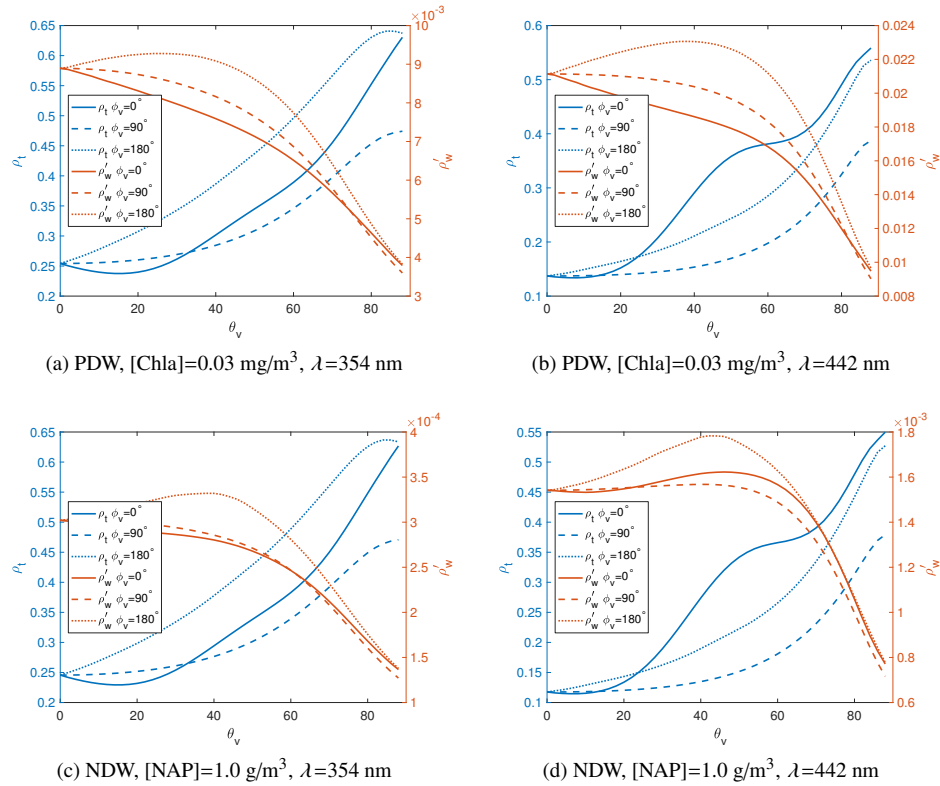


Fig. 3. Reflectance at the TOA as a function of viewing angle for selected wavelengths. Both the total reflectance and the water-leaving signal are shown. The solar zenith angle is 45° and the aerosol optical depth at 550 nm is 0.15.

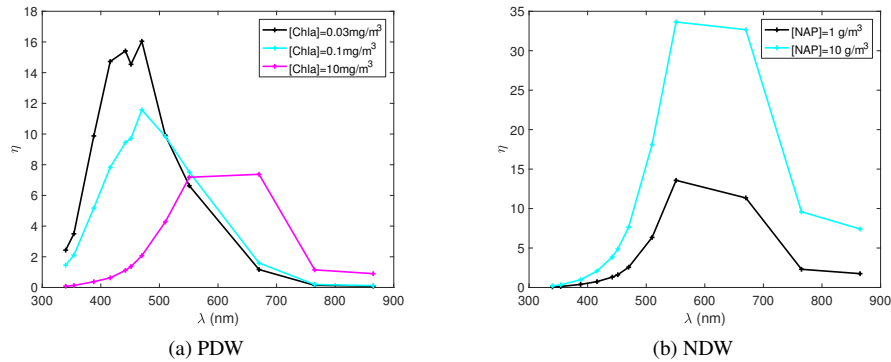


Fig. 4. Water-leaving contribution in the TOA reflectance at nadir as a function of wavelength. The solar zenith angle is 45° and the aerosol optical depth at 550 nm is 0.15.

viewing zenith angle with scales denoted by white numbers along a radius; the angular coordinate shows the viewing azimuth angle, with scales denoted by the black numbers from 0 to 180° around the semicircle. The azimuth angle of 0° corresponds to the azimuth half plane which contains the sun glint; while the azimuth angle 180° refers to the backscattering half plane. For PDW, [Chla] is 0.03 mg/m^3 ; for NDW, [NAP] = 1.0 g/m^3 and [Chla] = 10 mg/m^3 are used. The angular patterns of ρ_t for both PDW and NDW are similar, as the atmosphere is the same for the two cases and water leaving signal is relatively a small portion of the total signal. The total reflectance ρ_t is generally small at nadir in comparison with large viewing zenith angles, with the exact minimum value location determined by the atmospheric and oceanic phase matrices. For the water leaving signal, ρ'_w is smallest at large viewing zenith angles due to increasing atmospheric attenuation. The maximum water leaving signal is in the backscattering plane but not located at the exact backscattering direction of $\theta_v = 45^\circ$ and $\phi_v = 180^\circ$ due to the complicated interaction of light multiple scattering and atmospheric attenuation, which was also observed in [15].

To have a direct sense of the reflectance magnitude, Fig. 3 shows the line plots of ρ_t and ρ'_w as a function of viewing zenith angle θ_v for two selected wavelengths: 354 nm and 442 nm. The chlorophyll a concentration is 0.03 mg/m^3 for the PDW in Fig. 3; for NDW, [Chla] = 10 mg/m^3 and [NAP] = 1 g/m^3 are used. Three viewing azimuth angles are used: $0, 90, 180^\circ$. Consistent with the fisheye contour plot of the total reflectance ρ_t increases with increasing viewing zenith angle due to the increasing atmospheric path length. The water-leaving signal ρ'_w , however, decreases as θ_v increases, because of the larger atmospheric attenuation from larger atmospheric path length. This means that the water-leaving signal at nadir is usually largest among signals at different viewing angles at the TOA, both in absolute and relative measures. The sun glint at 354 nm is not obvious from the total reflectance ρ_t due to the large molecular scattering optical depth; while at 442 nm, the sun glint is apparent around $\theta_v = 45^\circ$ at $\phi_v = 0^\circ$, as $\theta_s = 45^\circ$ is used in this paper. The sun glint peak may also contain contributions from diffuse scattering [107].

The total reflectance shows larger variation for the three azimuth angles; while the water-leaving signal shows much smaller azimuth variation in Fig. 3. For PDW, ρ'_w is the largest at the backscatter plane $\phi_v = 180^\circ$, which gradually decreases as ϕ_v approaches zero. This has been observed in Fig. 2. However, this is not true for turbid NDW ([NAP] = 10 g/m^3 and $\lambda = 442 \text{ nm}$), in which the relative magnitude of ρ'_w at different ϕ_v changes depending on the viewing zenith angle. Similar variability of ρ'_w on azimuth angle has been observed in [15], depending

on [Chla] and wavelength. The ρ'_w maximum value at 354 nm is around $9\text{E-}3$ for PDW with [Chla]= 0.03 mg/m^3 , which is around 40% of the 442nm water leaving signal. For NDW and [NAP]= 1 g/m^3 , the maximum value of ρ'_w at 354 nm is $3.5\text{E-}4$, which is around 20% of the corresponding maximum value at 442 nm. This fraction of 20% is smaller than that of PDW, due to the strong [NAP] absorption in the UV. The CDOM absorption at 354 nm is less for PDW than NDW in this case due to the smaller [Chla] in PDW.

Besides the absolute signal, it is important to understand the relative fraction of water-leaving contribution in the total reflectance. Figure 4 shows the relative fraction $\eta = 100 \cdot \rho'_w / \rho_t$ for both PDW and NDW at nadir. For PDW, the maximum fraction ranges from 8% to 16%, and the wavelength corresponding to the maximum fraction shifts from 470 nm to 670 nm as [Chla] increases from 0.03 to 10 mg/m^3 . At both sides of the maximum peak, the fraction decreases as wavelength decreases toward the UV or increases toward NIR. The fraction is around or less than 2% at wavelengths shorter than 354 nm or longer than 760 nm. For NDW, the maximum fraction happens around 550 nm, which is not sensitive to the [NAP] value. The maximum fraction changes from around 15% to 35% when [NAP] increases from 1 g/m^3 to 10 g/m^3 . As wavelength approach UV, the fraction decreases at a faster rate than that of PDW due to the [NAP] absorption. In the NIR, the water-leaving fraction is still significant for NDW, which is around 8% or less at nadir. This is the reason that black pixel approximation in atmospheric correction fails in coastal waters [6].

Table 1. Maximum values of ρ'_w and η for all range of viewing zenith and azimuth angles of the TOA water leaving signal for PDW. The first column shows the [Chla] values.

λ		354 nm	388 nm	442 nm	765 nm	865 nm
0.03 mg/m ³	max(ρ'_w)	9.28E-3	2.11E-2	2.31E-2	3.48E-5	1.51E-5
	max(η)	3.60%	10.1%	15.6%	0.15 %	0.09%
0.1 mg/m ³	max(ρ'_w)	5.51E-3	1.05E-2	1.32E-2	4.74E-5	2.21E-5
	max(η)	2.17%	5.28%	9.54%	0.20%	0.13%
10 mg/m ³	max(ρ'_w)	3.31E-4	7.17E-4	1.40E-3	2.89E-4	1.75E-4
	max(η)	0.135%	0.39%	1.13%	1.18%	0.94%

Table 2. Maximum values of ρ'_w and η for all range of viewing zenith and azimuth angles of the TOA water leaving signal for NDW. The first column shows the [NAP] values.

λ		354 nm	388 nm	442 nm	765 nm	865 nm
1 g/m ³	max(ρ'_w)	3.32E-4	7.91E-4	1.78E-3	6.72E-4	3.89E-4
	max(η)	0.13%	0.40%	1.34%	2.38%	1.84%
10 g/m ³	max(ρ'_w)	9.55E-4	2.15E-3	5.52E-3	3.15E-3	1.87E-3
	max(η)	0.35%	1.03%	4.02%	9.88%	7.78%

Tables 1 and 2 summarize the maximum values of ρ'_w and η for PDW and NDW, respectively, for selected wavelengths. For each wavelength, the maximum values of ρ'_w and η for all range of viewing zenith and azimuth angles are reported. The magnitude of values in Tables 1 and 2 are consistent with the values in Figs. 1 and 4, because the maxima of water leaving signal and contribution are normally located at nadir, as suggested by Fig. 3.

3.2. Polarized reflectance

The polarized reflectance is very important for characterizing aerosol properties and has the potential to help atmospheric correction for ocean color imagery. Figure 5 shows the polarized

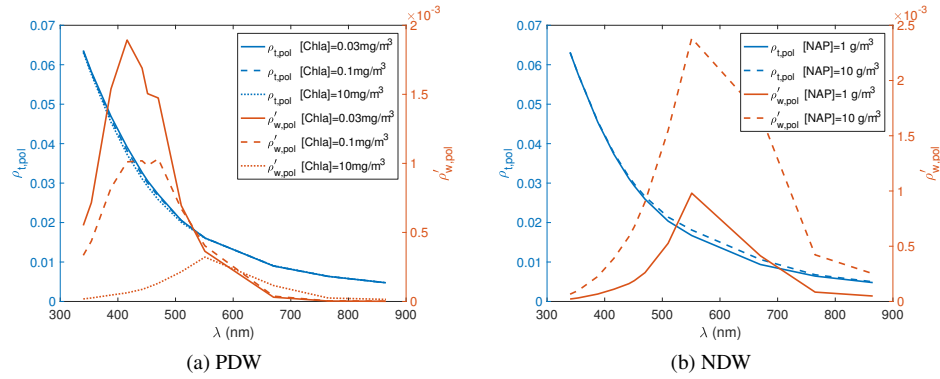


Fig. 5. TOA Polarized reflectance at nadir as a function of wavelength. Both the TOA polarized reflectance and the polarized water-leaving signal are shown. The solar zenith angle is 45° and the aerosol optical depth at 550 nm is 0.15.

reflectance for the same CAOS shown in Fig. 1. The wavelength dependence of the polarized reflectance at nadir is similar to that of the total reflectance, except that the magnitudes are much smaller. For PDW at 354 nm, $\rho_{t,pol}$ is around 0.065 regardless of the [Chla] value, while the corresponding ρ_t value is 0.28 as in Fig. 1. The degree of linear polarization (DOLP) is approximately $0.065/0.28=0.23$ at nadir. For polarized water-leaving signal, $\rho'_{w,pol}$ for [Chla]=0.03 mg/m^3 at 354 nm is around $2.0\text{E}-3$, while the corresponding ρ'_w in Fig. 1 is 0.025. This suggests that the water-leaving signal DOLP is around 0.08 at nadir, which is smaller than the total radiation field DOLP. Overall the DOLP for the total field is 2-3 times larger than the water-leaving signal, which is the main motivation of using the polarized reflectance for aerosol retrieval and atmospheric correction.

For PDW, the maximum $\rho'_{w,pol}$ in Fig. 5 is around $2\text{E}-3$ for [Chla]=0.03 mg/m^3 , which decreases to $2.5\text{E}-4$ for [Chla]=10 mg/m^3 . For NDW, the maximum $\rho'_{w,pol}$ values are $1.0\text{E}-3$ and $2.5\text{E}-3$, for [NAP]=1 and 10 g/m^3 , respectively. The polarized water-leaving signal $\rho'_{w,pol}$ is small in both UV and NIR due to strong CDOM and [NAP] absorption in UV and water absorption in NIR. For the cases shown, the $\rho'_{w,pol}$ value is around or smaller than $5\text{E}-4$ at 354 nm, which is near the detection limit of most ocean color sensors [20]. This suggests that one may use the polarized reflectance at 354 nm and nearby UV bands to perform atmospheric correction by assuming the water-leaving signal is small and well constrained and identifying aerosol types and optical depths.

To understand the angular dependence of the polarized reflectance, Fig. 6 shows the fisheye projection contour plot of $\rho_{t,pol}$ and $\rho'_{w,pol}$ and for both PDW and NDW. For PDW, [Chla]=0.03 mg/m^3 is used, and for NDW, [NAP]=1.0 g/m^3 is used. The minimum polarized reflectances for both $\rho_{t,pol}$ and $\rho'_{w,pol}$ appear around the backscattering direction of $\theta_v = 45^\circ$ and $\phi_v = 180^\circ$. As viewing zenith angle approaches 90° , $\rho_{t,pol}$ increases while $\rho'_{w,pol}$ decreases, for the same reason as the case of ρ_t and ρ'_w , i.e., increasing scattering path length for the total field and attenuation path length for water leaving signal. The angular pattern of $\rho_{t,pol}$ is similar for both PDW and NDW due to the dominant contribution of the atmospheric signal. The water leaving signals for PDW and NDW show different maximum reflectance and angular distribution, with the PDW peak exhibiting a larger angular area in the principal plane around the scattering angle of 90° . The NDW peak is comparably narrower due to the PDW and NDW phase matrix

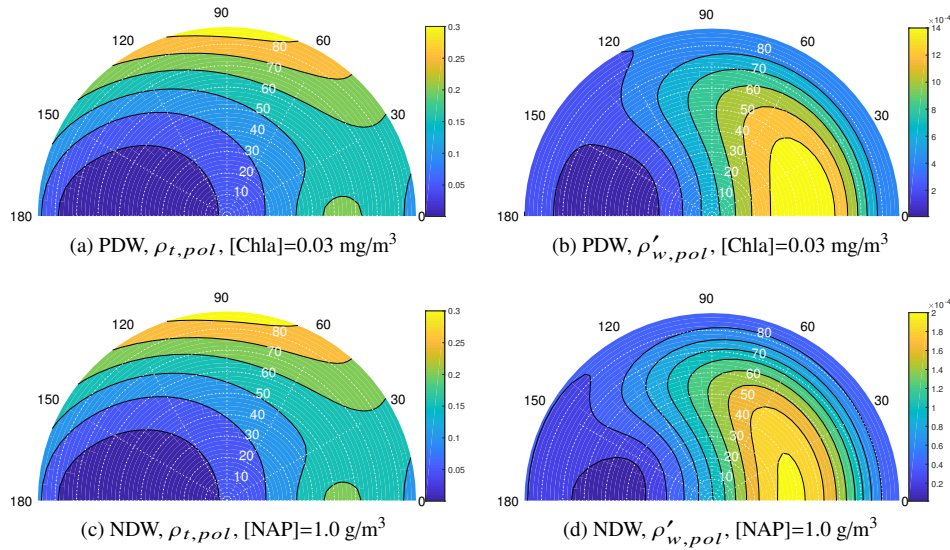


Fig. 6. Fisheye contour plot of the TOA polarized reflectance as a function of viewing angle at 354 nm. Both the TOA polarized reflectance and the polarized water-leaving signal are shown. The solar zenith angle is 45° and the aerosol optical depth at 550 nm is 0.15.

difference. These characterizations have a potential to be used for ocean color atmospheric correction using multiangle polarimetry.

In comparison to the total reflectance, the polarized reflectance shows much larger angular variation for different cases, which prompts us to examine the polarized reflectance in a greater detail. Figure 7 shows the polarized reflectance for PDW as a function of viewing zenith angles for three azimuth angles: $\phi_v = 0, 90, 180^\circ$. Two [Chla] values, 0.03 and 10 mg/m^3 are used; and the wavelengths are 354 and 442 nm. For both $\rho_{t,pol}$ and $\rho'_{w,pol}$, the maximum values are at $\phi_v = 0^\circ$ around the scattering angle of 90° ; the minimum values are at $\phi_v = 180^\circ$. This is consistent with the synoptic view reported in [15]. For [Chla] = 0.03 mg/m^3 , the $\rho'_{w,pol}$ maxima are $1.6\text{E-}3$ and $5\text{E-}3$ for the wavelengths of 354 and 442 nm, respectively. For [Chla] = 10 mg/m^3 , the $\rho'_{w,pol}$ maxima are $6\text{E-}5$ and $3\text{E-}4$ for 354 nm and 442 nm, respectively. Overall the $\rho'_{w,pol}$ values are smaller for [Chla] = 10 mg/m^3 than those for [Chla] = 0.03 mg/m^3 for $\lambda < 550$ nm. In the principal plane of $\phi_v = 0^\circ$, the relative differences between $\rho'_{w,pol}(\theta_v = 0^\circ)$ and the $\rho'_{w,pol}$ maximum are around 100%. At $\phi_v = 90^\circ$, the $\rho'_{w,pol}$ variations are more smooth as a function of viewing zenith angle.

Figure 8 is the same as Fig. 7, except for NDW. Two [NAP] values, 1 and 10 g/m^3 , are used. The angular variations of the polarized reflectance for NDW are similar to those of PDW, i.e., maximum values are at $\phi_v = 0^\circ$ and minimum values are at $\phi_v = 180^\circ$. In comparison with PDW, the viewing zenith angle of the $\rho'_{w,pol}$ maximum at $\phi_v = 0^\circ$ appears closer to the zenith (40° versus 45°). This is due the Mueller matrix difference of the PDW and NDW. In PDW, the average reduced Mueller matrix measured by Voss and Fry are used [72], in which the P_{12}/P_{11} has a maximum around 90° . For NDW, the Mie theory is used to calculate the particle Mueller matrix, whose P_{12}/P_{11} maximum deviates from 90° , especially for non-algae particles with high refractive index particles [79].

For NDW with [NAP] = 1.0 g/m^3 at 354 nm, $\rho'_{w,pol}$ at $\phi_v = 0^\circ$ changes from $3\text{E-}5$ to $7.5\text{E-}5$

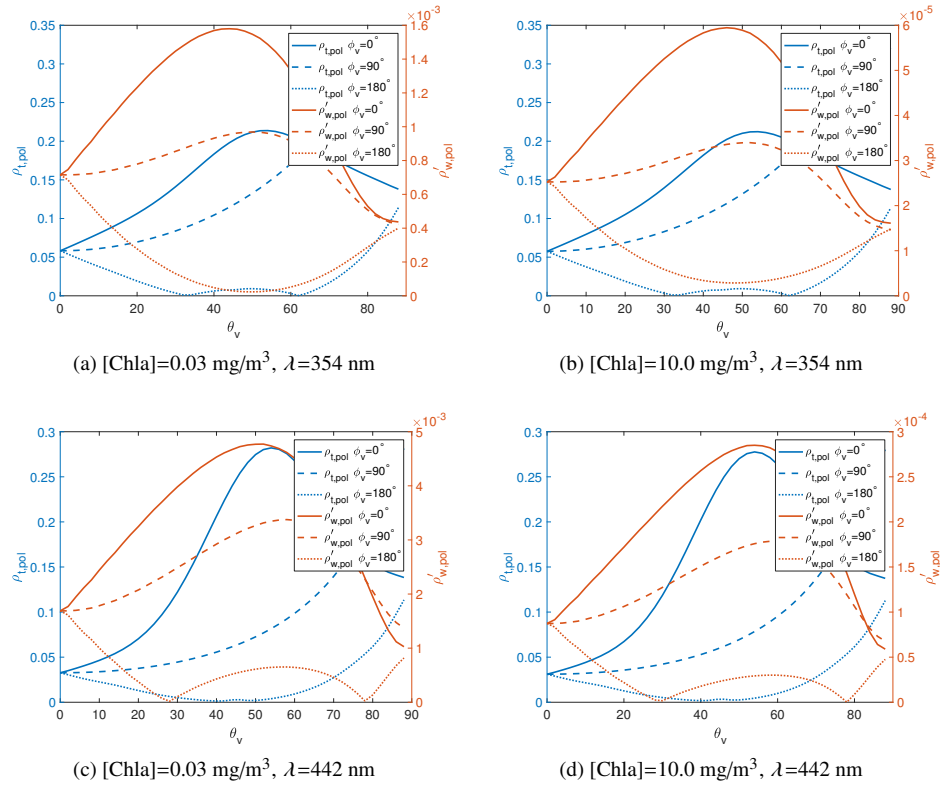


Fig. 7. TOA polarized reflectance for PDW as a function of viewing angle for selected wavelengths. Both the total field and the water-leaving signal are shown. The solar zenith angle is 45° and the aerosol optical depth at 550 nm is 0.15.

when the viewing zenith increases from 0 to 45°, an increase of more than 100%. For the wavelengths from 354 nm to 442 nm, the $\rho'_{w, pol}$ maxima for [NAP]=1.0 g/m³ in Fig. 8 range from approximately 2.0E-4 to 5E-4. For [NAP]=10.0 g/m³, the $\rho'_{w, pol}$ maxima are between 2E-4 to 1.5E-3 for the wavelengths from 354 nm to 442 nm. The $\rho'_{w, pol}$ maxima for NDW are in the same order of magnitude as those of PDW. At 354 nm, the maximum values are again smaller than 5E-4, which confirms that polarized measurements at 354 nm will be a powerful band for characterizing aerosol properties and performing atmospheric correction, by assuming a small fraction of water leaving contribution at this wavelength.

To show the polarized water leaving contribution to the TOA polarized reflectance, Fig. 9 shows $\eta_{pol} = 100 \cdot \rho'_{w, pol} / \rho_{t, pol}$ at nadir as a function of wavelength. The spectral behavior of the polarized water leaving fraction is similar to that of the total reflectance, with the wavelength of the PDW maximum fraction strongly depending on [Chla] and with the wavelength of the NDW maximum fraction less sensitive to [NAP]. The PDW maximum fraction is larger for smaller [Chla]; while the NDW maximum fraction is larger for larger [NAP]. The PDW maximum fraction ranges from 2% to 5.5% for [Chla] decreasing from 10 to 0.03 mg/m³; while the NDW maximum fraction ranges from 6% to 16% for [NAP] increasing from 1 to 10 g/m³.

Different from the total reflectance, the polarized water leaving contribution has more complicated angular pattern. Figure 10 shows $\eta_{pol} = 100 \cdot \rho'_{w, pol} / \rho_{t, pol}$ for both PDW and NDW as a

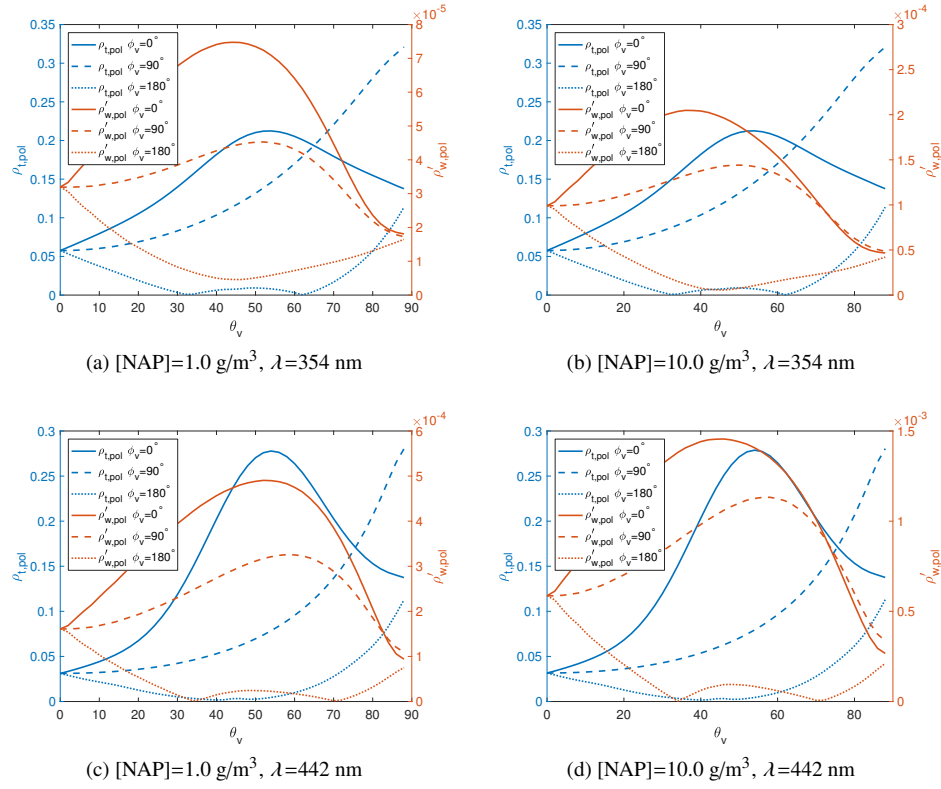


Fig. 8. TOA polarized reflectance for NDW as a function of viewing angle for selected wavelengths. Both the total field and the water-leaving signal are shown. The solar zenith angle is 45° and the aerosol optical depth at 550 nm is 0.15.

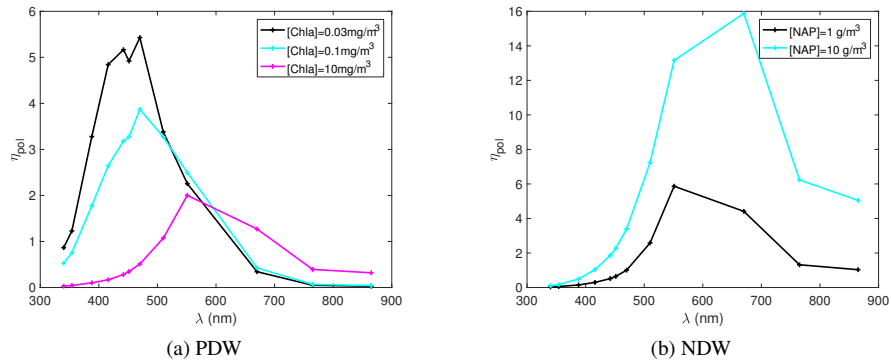


Fig. 9. Polarized water-leaving contribution in the TOA polarized reflectance at nadir as a function of wavelength. The solar zenith angle is 45° and the aerosol optical depth at 550 nm is 0.15.

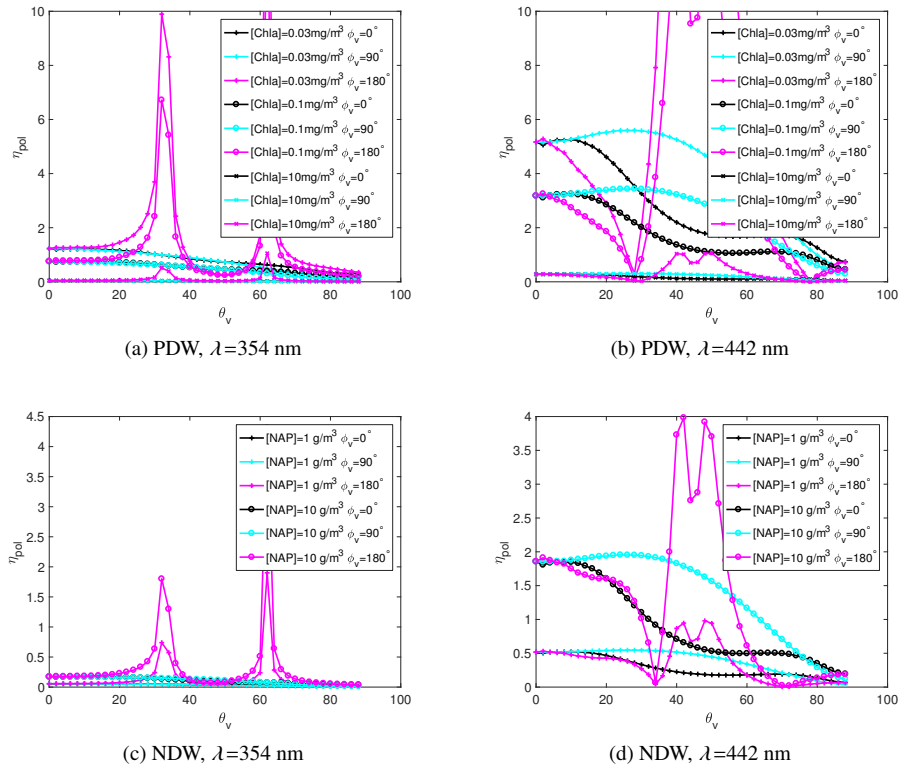


Fig. 10. Water-leaving contribution to the TOA polarized reflectance as a function viewing angles for selected wavelengths. The solar zenith angle is 45° and the aerosol optical depth at 550 nm is 0.15.

function of viewing zenith angle for three azimuth angles. At 354 nm, the fraction is in general smaller than 2% except for $\phi_v = 180^\circ$. In the backscattering plane the polarized reflectance is minimized for both $\rho_{t,pol}$ and $\rho'_{w,pol}$, which leads to numerical instability when calculating the ratio of two small numbers. When the backscattering half plane is excluded, the fraction is smaller than 6% at 442 nm. While the angular variations of $\rho'_{w,pol}$ and $\rho_{t,pol}$ are large (i.e., Figs. 7 and 8), the fraction η_{pol} shows little angular dependence except for the backscattering plane. Moreover, the fraction is generally maximized at nadir, and slowly decreases to zero for large viewing zenith angles. All these facts can be used as constraints to develop new atmospheric correction algorithms in least squares fitting of the multi-angle polarimeter measurements.

Table 3 and 4 summarize the maximum values of $\rho'_{w,pol}$ and η_{pol} for PDW and NDW, respectively, for selected wavelengths. The maximum values of $\rho'_{w,pol}$ apply to all range of viewing zenith and azimuth angles. For η_{pol} , the backscattering direction between $\phi_v = 150^\circ$ and 180° are however excluded to avoid numerical instability as we discussed above. The relative contribution for PDW at 865 nm is in general smaller than 1%. This is not the case for NDW, in which η_{pol} could be up to 8.17% as shown in Table 4 for $[NAP]=10 \text{ g/m}^3$. Noticeably, the polarized water leaving contributions at 354 nm and 388 nm are smaller than those of 765 nm and 865 nm, which makes the UV bands a better choice for atmospheric correction for turbid NDW.

Table 3. Maximum values of $\rho'_{w,pol}$ and η_{pol} of the TOA water leaving signal for PDW. The maximum value of η_{pol} only includes viewing azimuth angles between 0 and 150°. The first column shows the [Chla] values.

	λ	354 nm	388 nm	442 nm	765 nm	865 nm
0.03 mg/m ³	$\max(\rho'_{w,pol})$	1.58E-3	3.80E-3	4.77E-3	1.29E-5	6.14E-6
	$\max(\eta_{pol})$	1.26%	3.35%	8.59%	0.10%	0.05%
0.1 mg/m ³	$\max(\rho'_{w,pol})$	9.76E-4	2.07E-3	2.98E-3	1.94E-5	9.92E-6
	$\max(\eta_{pol})$	0.77%	1.82%	5.10%	0.13%	0.08%
10 mg/m ³	$\max(\rho'_{w,pol})$	5.95E-5	1.25E-4	2.85E-4	1.41E-4	9.04E-5
	$\max(\eta_{pol})$	0.05%	0.10%	0.44%	0.73%	0.58%

Table 4. Maximum values of $\rho'_{w,pol}$ and η_{pol} of the TOA water leaving signal for NDW. The maximum value of η_{pol} only includes viewing azimuth angles between 0 and 150°. The first column shows the [NAP] values.

	λ	354 nm	388 nm	442 nm	765 nm	865 nm
1 g/m ³	$\max(\rho'_{w,pol})$	7.48E-5	1.78E-4	4.90E-4	3.70E-4	2.21E-4
	$\max(\eta_{pol})$	0.06%	0.15%	0.76%	2.37%	1.75%
10 g/m ³	$\max(\rho'_{w,pol})$	2.05E-4	5.06E-4	1.46E-3	1.30E-3	7.85E-4
	$\max(\eta_{pol})$	0.18%	0.52%	2.92%	11.2%	8.17%

4. Conclusion

In this paper we have systematically investigated the water-leaving absolute signal and relative contribution in both total and polarized reflectances at TOA. The spectrum ranges from UV to NIR, which covers all spectral bands in which water-leaving radiance has noticeable contribution to the TOA radiation field. Bio-optical models for both PDW and NDW are included in this study. The PDW IOPs are primarily determined by chlorophyll a concentration, while those of NDW have an additional non-algae component that both scatters and absorbs light. The radiative transfer model based on the successive order of scattering method is used to perform the simulation, in which polarization, atmosphere and ocean coupling, and elastic and inelastic scattering are included. Main inelastic scattering mechanisms are Raman scattering and fluorescence by dissolved organic matter.

For the total reflectance in PDW, the wavelength of the maximum water-leaving signal shifts from 412 nm to 550 nm when chlorophyll a concentration increases from 0.03 to 10 mg/m³. This is not the case for NDW, in which the wavelength of the maximum water-leaving signal does not change with different non-algae concentrations. The maximum reflectance for PDW is larger for smaller chlorophyll a concentrations, while the reflectance in NDW is in general larger for larger non-algae concentrations. As viewing zenith angle increases, the water-leaving signal decreases for both PDW and NDW, which is due to the increase of atmospheric attenuation path. On the other hand, the total reflectance for the whole CAOS increases as viewing zenith angle increases, which makes the water-leaving relative contribution in the total field decreases quickly towards large viewing zenith angles. The water-leaving signal is small in both UV and NIR. At 354 the water-leaving fraction in the total reflectance is less than 4% and 0.5% for PDW and NDW, respectively. At 865 nm, the water-leaving fraction for PDW is smaller than 1%. This fraction is around 8% for turbid NDW ([NAP]=10 g/m³).

For the TOA polarized field, the spectral variation is similar to that of the total reflectance, with much smaller magnitude. The DOLP of the whole CAOS is normally 2-3 times larger than

the water-leaving signal, which means that the TOA polarized field is dominated by atmospheric scattering. The polarized reflectance is expected to show maximum values in the principle half plane, which contains the sun glint. The minimum polarization is around the backscattering half plane. The polarization peak is around the scattering angle of 90° for PDW. The peak location is shifted away from 90° for NDW, depending on the single scattering Mueller matrix, which in turn depends on the refractive index and particle size distributions. If the backscattering half plane is excluded, the water-leaving contribution in the polarized field is less than 2% at 354 nm and 9% at 442 nm, for both PDW and NDW. In the backscattering plane, the fraction is larger due to the numerical instability of dividing two near-zero numbers (both polarized water-leaving and total signals are minimized in the backscattering plane). The relative and absolute magnitudes of these different contributions in PDW and NDW will provide important guidelines in designing new aerosol retrieval and atmospheric correction algorithms for the future satellite missions by allowing a better separation of the water and aerosol contributions to the TOA signal.

Funding

NASA (NNX15AB94G and NNX15AK87G)

Acknowledgment

Pengwang Zhai is partially supported by the NASA PACE Project. This study is also partially supported by the NASA Radiation Science program administrated Hal Maring and the Biology and Biogeochemistry program administrated by Paula Bontempi.